

TWO- AND THREE-DIMENSIONAL SIMULATIONS OF ASTEROID OCEAN IMPACTS

LA-UR 02-66-30

Galen Gisler, Robert Weaver, Charles Mader
Los Alamos National Laboratory
Los Alamos, NM, USA

Michael Gittings
Science Applications International
Los Alamos, NM, USA

We have performed a series of two-dimensional and three-dimensional simulations of asteroid impacts into an ocean using the SAGE code from Los Alamos National Laboratory and Science Applications International Corporation. The SAGE code is a compressible Eulerian hydrodynamics code using continuous adaptive mesh refinement for following discontinuities with a fine grid while treating the bulk of the simulation more coarsely. We have used realistic equations of state for the atmosphere, sea water, the oceanic crust, and the mantle. In two dimensions, we simulated asteroid impactors moving at 20 km/s vertically through an exponential atmosphere into a 5 km deep ocean. The impactors were composed of mantle material (3.32 g/cc) or iron (7.8 g/cc) with diameters from 250m to 10 km. In our three-dimensional runs we simulated asteroids of 1 km diameter composed of iron moving at 20 km/s at angles of 45 and 60 degrees from the vertical. All impacts, including the oblique ones, produce a large underwater cavities with nearly vertical walls followed by a collapse starting from the bottom and subsequent vertical jetting. Substantial amounts of water are vaporized and lofted high into the atmosphere. In the larger impacts, significant amounts of crustal and even mantle material are lofted as well. Tsunamis up to a kilometer in initial height are generated by the collapse of the vertical jet. These waves are initially complex in form, and interact strongly with shocks propagating through the water and the crust. The tsunami waves are followed out to 100 km from the point of impact. Their periods and wavelengths show them to be intermediate type waves, and not (in general) shallow-water waves. At great distances, the waves decay as the inverse of the distance from the impact point, ignoring sea-floor topography. For all impactors smaller than about 2 km diameter, the impacting body is highly fragmented and its remains lofted into the stratosphere with the water vapor and crustal material, hence very little trace of the impacting body should be found for most oceanic impacts. In the oblique impacts, the initial asymmetry of the transient crater and crown does not persist beyond a tsunami propagation length of 50 km.

1. Introduction

On a geological time scale, impacts of asteroids and comets with the earth must be considered as a relatively frequent occurrence, causing significant disturbances to biological communities and strongly perturbing the course of evolution. For a review of much of this work, see Pierazzo and Melosh, 2000, *Ann. Rev. Earth Planet. Sci.* 28:141. Most famous among catastrophic impacts, of course, is the one that marked the end of the Cretaceous period and the dominance of the dinosaurs.

It is now widely accepted that the worldwide sequence of mass extinctions at the Cretaceous-Tertiary (K-T) boundary 65 million years ago was directly caused by the collision of an asteroid or comet with the earth (see, e.g. Morgan et al, 2000, *Earth and Planetary Science Letters* 183:347; and Pierazzo et al., 1998, *Journal of Geophysical Research* 103:28607). Evidence for this includes the large (200 km diameter) buried impact structure at Chicxulub, Yucatan, Mexico, the world-wide distributed Iridium layer at the K-T boundary, and tsunamic deposits well inland in North America, all dated to the same epoch as the extinction event.

Consensus is building (a) that the K-T impactor was a bolide of diameter roughly 10 km, (b) that its impact was oblique (not vertical), either from the SE at 30 degrees to the horizontal or from the SW at 60 degrees, and (c) that its encounter with layers of water, anhydrite, gypsum, and calcium carbonate (all highly volatile materials at the pressures of impact) resulted in the lofting of many hundreds of cubic kilometers of these materials into the stratosphere where they resided for many years and produced a global climate deterioration that was fatal to many large-animal species on earth. All of these points are still under discussion, however, and the scientific questions that still need to be answered are (for example):

(1) How is the energy of impact (in the realm of a million gigatons TNT equivalent) partitioned among the vaporization of volatiles, the generation of tsunamis, and the cratering of the substrate? How is this partition of energy reflected in the observables detectable after 65 million years?

(2) What is the fate of the projectile?

(3) How do (1) and (2) depend upon the unknown parameters of the problem, namely bolide mass, velocity, and angle of impact?

In preparation for a definitive simulation of large events like Chicxulub, we have undertaken a program of modeling smaller impacts, beginning with impacts in the deep ocean where the physics is somewhat simpler. Smaller impacts happen more frequently than the "dinosaur-killer" events, and there is evidence in the geological record for impactors of ~2 km diameter off the coast of Chile (the Eltanin event, e.g. Kyte, 2002, *Deep Sea Research II* 49:1049) and in the North Sea (Stewart & Allen, 2002, *Nature* 418:820). Besides sea-floor cratering, these events will give rise to tsunamis (e.g. Ward & Asphaug, 2002, *Deep Sea Research II* 49:1073) that leave traces many kilometers inland from a coast facing the impact point.

We devote our attention in this paper to these smaller impacts, and concentrate first on

oceanic events. The same questions need to be answered as for the larger events.

This work follows on, and is influenced by, the work of Mader and Gittings (2003) on water cavity generation reported in this volume.

2. The Code

The SAGE hydrocode is an adaptive grid eulerian code with a high-resolution Godunov scheme originally developed by M.L. Gittings for Science Applications International (SAIC) and Los Alamos National Laboratory (LANL). It uses continuous adaptive mesh refinement (CAMR) by which we mean that the decision to refine the grid is made cell-by-cell and cycle-by-cycle continuously throughout the problem run. With the computing power concentrated on the regions of the problem which require high resolution, much larger computational volumes can be simulated at low cost.

It can be run in several modes of geometry and dimensionality, explicitly 1-D Cartesian and spherical, 2-D Cartesian & cylindrical, and 3-D Cartesian. A separate module for implicit, gray, non-equilibrium radiation diffusion is available but was not used in these calculations.

Because modern supercomputing is commonly done on machines or machine clusters containing many identical processors, the parallel implementation of the code is supremely important. For portability and scalability, SAGE uses the widely available Message Passing Interface (MPI). Load leveling is accomplished through the use of an adaptive cell pointer list, in which newly created daughter cells are placed immediately after the mother cells. Cells are redistributed among processors at every time step, while keeping mothers and daughters together. If there are a total of M cells and N processors, this techniques gives very nearly M/N cells per processor. As neighbor-cell variables are needed, the MPI gather/scatter routines copy those neighbor variables into local scratch.

The code incorporates multiple material equations of state (analytical or tabular) with a variety of strength models, and every cell can in principle contain a mixture of all the materials in the problem. For the asteroid ocean impact problems we used 5 materials in the problem. The first four of these are the same for all our simulations, namely air, water, basalt for the oceanic crust, and garnet for the mantle material underneath the oceanic crust. The fifth material, for the asteroid, was taken to be either dunite (3.32 g/cc) as a mockup for typical stony asteroids, or steel (7.81 g/cc) as a mockup for nickel-iron asteroids. We used tabular equations of state for the air, water, basalt, and garnet, and Mie-Grüneisen equations of state for the dunite and steel. The strength model used for the crust and asteroid are the same in all cases, namely an elasto-plastic model with shear moduli and yield stress similar to experimental values for aluminum. Only in our larger impacts is the crust penetrated, and in these we require the mantle material to have strength properties as well. For the known increase of strength with depth we use a simple pressure-hardening relationship.

3. The Simulations

Three-dimensional simulations of a 1-km diameter iron asteroid impacting the ocean at a 45-degree angle at 20 km/s were performed on the ASCI White machine at Lawrence Livermore National Laboratory, using up to 1200 processors for several weeks. Up to 200,000,000 computational cells were used, and the total computational time was 1,300,000 cpu-hours. The computational volume was a rectangular box 200 km long in the direction of the asteroid trajectory, 100 km wide, and 60 km tall. The height was divided into 42 km of atmosphere, 5 km ocean water, 7 km basalt crust, and 6 km mantle material. Using bilateral symmetry, we simulated a half-space only, the boundary of the half-space being the vertical plane containing the impact trajectory.

The asteroid is started at a point 30 km above the surface of the water (see Figure 1). The atmosphere used in this simulation is a standard exponential atmosphere, so the medium surrounding the bolide is very tenuous (density ~1.5% of sea level density) when the calculation begins. During the 2.1 seconds of the bolide's atmospheric passage at ~Mach 60, a strong shock develops, heating the air to temperatures upwards of 1 eV (1.2×10^4 K). Less than 1% of the bolide's kinetic energy (roughly 1500 Gigatons high explosive equivalent yield) is dissipated in the atmospheric passage.

The water is much more effective at slowing the asteroid, and essentially all of its kinetic energy is absorbed by the ocean and seafloor within 0.7 seconds. The water immediately surrounding the trajectory is vaporized, and the rapid expansion of the vapor cloud excavates a cavity in the water that eventually expands to a diameter of 25 km. This initial cavity is asymmetric because of the inclined trajectory of the asteroid, and the splash, or crown, is markedly higher on the side opposite the incoming trajectory (the downstream side, see Figure 2). The maximum height of the crown on the downstream side is nearly 30 km at 70 seconds after impact. The collapse of the bulk of the crown makes a "rim wave" or precursor tsunami that propagates outward, somewhat higher on the downstream side. The higher portion of the crown breaks up into droplets that fall back into the water giving this precursor tsunami a very uneven and asymmetric profile.

The rapid dissipation of the asteroid's kinetic energy is very much like an explosion, and acts to symmetrize the subsequent development. Shocks propagate outward from the cavity in the water, in the basalt crust and in the mantle beneath. Multiple reflections of shocks and acoustic waves between the material interfaces complicate the dynamics.

The hot vapor from the initial cavity expands into the atmosphere, mainly in the downstream direction because of the momentum of the asteroid (see Figure 3, which is from a run, still in progress, of a 30-degree impact). When the pressure of the vapor in the cavity has diminished sufficiently, at about 35 seconds after the impact, water begins to fill the cavity from the bottom, driven by pressure. This filling has a high degree of symmetry because of the uniform gravity responsible for the water pressure. An asymmetric fill could result from non-uniform seafloor topography, but that is not considered here. The filling water converges on the center of the cavity and the implosion produces another series of shock waves, and a jet that rises vertically in the atmosphere to a height in excess of 20 km at a time of 150 seconds after impact. It is the collapse of this central vertical jet that produces the principal tsunami wave (Figure 4).

We follow the evolution of this wave in three dimensions out to a time of 400 seconds after impact, and find that the inclined impact eventually produces a tsunami that is very nearly circularly symmetric at late times (Figure 5). The tsunami has an initial height in excess of 1 km, and declines to 100 meters at a distance of 40 km from the initial impact. Its propagation speed is 175 meters/second.

The 45-degree angle chosen for this 3-dimensional simulation is the most probable angle for impacts (Gilbert, 1893, *Bull. Philos. Cos. Wash.* 12:241). We have recently begun 3-dimensional simulations of a 30-degree impactor to better understand the dependence of the phenomenology on the angle of impact. However, because of the high degree of symmetry achieved late in the calculation, much can be learned about the physics of impact events by performing 2-dimensional simulations. Because these are much cheaper than full 3-dimensional calculations, full parameter studies can be undertaken to isolate the dependence of the phenomena on the properties of the impactor.

We have therefore performed a series of supporting calculations in two dimensions (cylindrical symmetry) for asteroids impacting the ocean vertically at 20 km/s, using the ASCI BlueMountain machines at Los Alamos National Laboratory. These simulations were designed to follow the passage of an asteroid through the atmosphere, its impact with the ocean, the cavity generation and subsequent re-collapse, and the generation of tsunami. The parameter study included 6 different asteroid masses. Stony and iron bodies of diameters 250 meters, 500 meters, and 1000 meters were used. The kinetic energies of the impacts ranged from 1 Gigatons to 200 Gigatons (high-explosive equivalent yield). An example montage from the two-dimensional parameter study is shown in Figure 6, for a 1-km iron bolide impacting vertically into a 5 km ocean. Comparison of this with Figure 1, shows that the cratering of the basalt crust is considerably enhanced for vertical impact. This is expected, since the shorter path length through the water implies less dissipation of the bolide's kinetic energy in the water before the encounter with the crust. Penetration depth may thus be an effective diagnostic of impact angle, provided other parameters can be independently determined.

A tabular summary of our parameter study is presented in Table I, in which are listed the input characteristics of the bolide (composition, diameter, density, mass, velocity and kinetic energy) and the measured characteristics of the impact (maximum depth and diameter of the transient cavity, quantity of water displaced, time of maximum cavity, maximum jet and jet rebound, tsunami wavelength and tsunami velocity).

The amount of water displaced during the formation of the cavity is found to scale very nearly linearly with the kinetic energy of the asteroid, as illustrated in Figure 8. A fraction of this displaced mass is actually vaporized during the explosive phase of the encounter, while the rest is pushed aside by the pressure of the vapor to form the crown and rim of the transient cavity.

The tsunami amplitude is also found to scale roughly linearly with the asteroid kinetic energy, and it evolves in a complex manner, eventually decaying rather faster than $1/r$ (where r is the distance of propagation from the impact point (Figure 9)). The wave trains are initially highly complex (see Figure 7) because of the multiple shock

reflections and interactions involving the seafloor. Realistic seafloor topography will undoubtedly influence the development of the wave.

It is expected that the tsunami waves will eventually evolve into classic shallow-water waves (e.g. Mader, *Numerical Modeling of Water Waves*) because the wavelengths are long compared to the ocean depth. However, the complexity of the initial wave train, and the wave-breaking associated with the interaction of shocks reflected from the seafloor, do not permit the simplifications associated with shallow-water theory. Much previous work on impact-generated tsunamis (e.g. Crawford & Mader, 1998, *Science of Tsunami Hazards* 16:21) has used shallow-water theory, which gives a particularly simple form for the wave velocity, namely $v = \sqrt{gD}$, where g is the acceleration due to gravity and D is the water depth. For an ocean of 5 km depth, the shallow-water velocity is 221 m/s. In Figure 9 we show the wave crest positions as a function of time for the simulations in our parameter study, along with constant-velocity lines at 150 and 221 m/s. From this it is seen that the wave velocities are substantially lower than the shallow-water limit, though there is some indication of an approach to that limit at late times. This asymptotic approach is only observed for the largest impactors because the waves from the smaller impactors die off too quickly for reliable measurement in our simulations. Better measurements, with tracer particles, are in progress.

The tsunami wavelength is found to scale roughly with the 1/4 power of the asteroid kinetic energy, as shown in Figure 10. The reason for this is that the wavelength is determined by the cavity-jet-rebound cycle, and the timescale for this goes as $(\langle h \rangle / g)$, where $\langle h \rangle$ is the mean jet height. The mean jet height, in turn, goes as the square root of the asteroid kinetic energy.

4. Recent developments and future plans

The study outlined in this paper is continuing, with a shift in focus to larger impacts and impacts in very shallow water (as at Chicxulub) and on land. For these more difficult runs it is very important to include a proper characterization of the material strength of the geological strata in which the impact occurs and the dependence of those strength properties with depth. This data is still not readily available, unfortunately. Nevertheless, we are making progress with these simulations, and hope to report on them soon.

Acknowledgments

We wish to thank Bob Greene for assistance with the visualization of the three-dimensional runs, and Anita Schwendt for help with the material strength characterization. We have also had helpful conversations with Eileen Ryan, Jay Melosh, Betty Pierazzo, Gareth Collins, and Tom Ahrens on the impact problem in general.

References

- Crawford & Mader, 1998, *Science of Tsunami Hazards* 16:21.
Gilbert, 1893, *Bull. Philos. Cos. Wash.* 12:241.
Kyte, 2002, *Deep Sea Research II* 49:1049.
Mader, 1988, *Numerical Modeling of Water Waves* University of California Press.
Mader & Gittings, 2003, *Science of Tsunami Hazards* 21:102.
Morgan et al, 2000, *Earth and Planetary Science Letters* 183:347.
Pierazzo and Melosh, 2000, *Ann. Rev. Earth Planet. Sci.* 28:141.
Pierazzo et al., 1998, *Journal of Geophysical Research* 103:28607.
Stewart & Allen, 2002, *Nature* 418:820.
Ward & Asphaug, 2002, *Deep Sea Research II* 49:1073.

Table I. Summary of parameter-study runs

Asteroid material	Dunite	Iron	Dunite	Iron	Dunite	Iron
Asteroid diameter	250 m	250 m	500 m	500 m	1000 m	1000 m
Asteroid density	3.32 g/cc	7.81 g/cc	3.32 g/cc	7.81 g/cc	3.32 g/cc	7.81 g/cc
Asteroid mass	2.72e13 g	6.39e13 g	2.17e14 g	5.11e14 g	1.74 e15 g	4.09e15 g
Asteroid velocity	20 km/s	20 km/s				
Kinetic energy	1.3 GT	3 GT	10 GT	24 GT	83 GT	195 GT
Maximum cavity diameter	4.4 km	5.2 km	10.0 km	12.6 km	18.6 km	25.2 km
Maximum cavity depth	2.9 km	4.3 km	4.5 km	5.7 km	6.6 km	9.7 km
Observed water displacement	4.41e16 g	9.13e16 g	3.53e17 g	7.11e17 g	1.79e18 g	4.84e18 g
Time of max cavity	13.5 s	16.0 s	22.5 s	28.0 s	28.5 s	33.0 s
Time of max jet	54.5 s	65.0 s	96.5 s	111 s	128.5 s	142 s
Time of rebound	100.5 s	118.5 s	137.5 s	162 s	187.5 s	218.5 s
Tsunami wavelength	9 km	12 km	17 km	20 km	23 km	27 km
Tsunami velocity	120 m/s	140 m/s	150 m/s	160 m/s	170 m/s	175 m/s

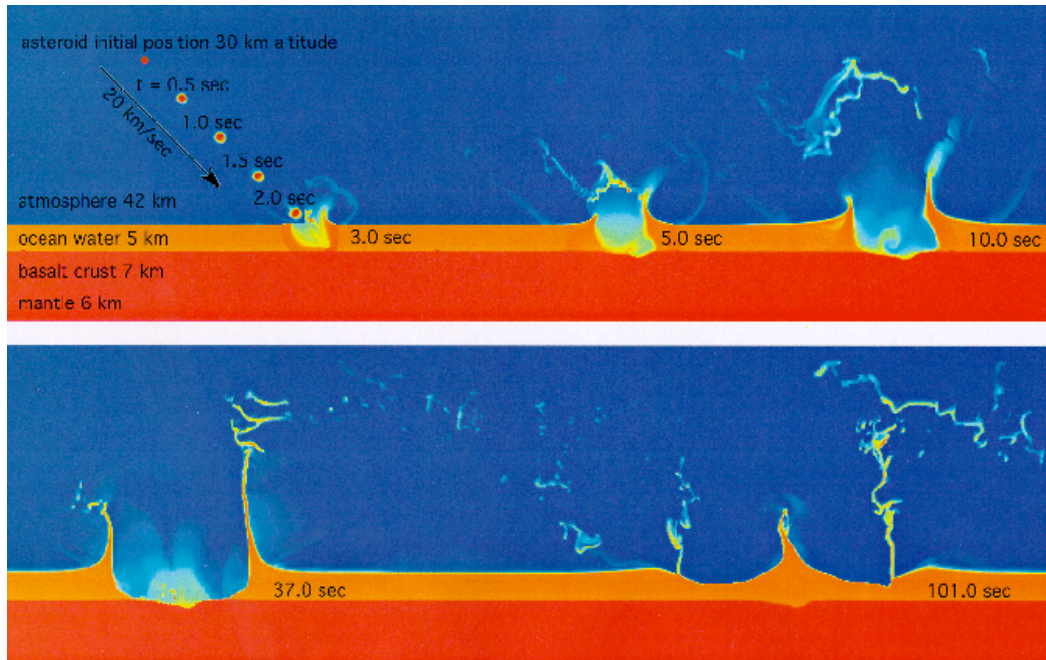


Figure 1. Montage of 9 separate images from the 3-d run of the impact of a 1-km iron bolide at an angle of 45 degrees with an ocean of 5-km depth. These are density raster graphics in a two-dimensional slice in the vertical plane containing the asteroid trajectory. Note the initial asymmetry and its disappearance in time.

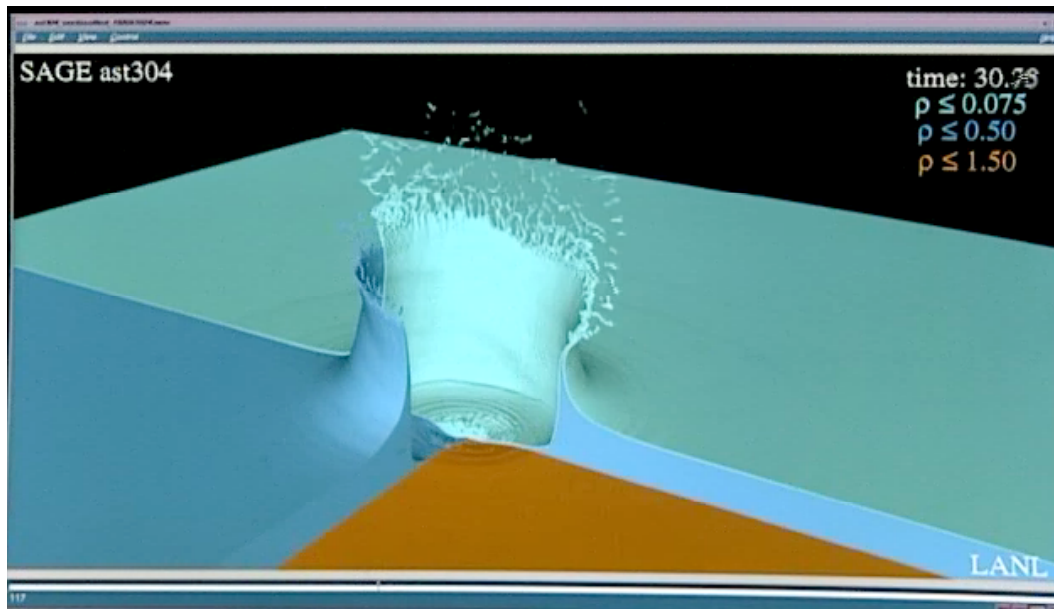


Figure 2. A perspective cutaway view from the same run illustrated in Fig. 1 at a time near the maximum cavity. The brown is the basalt crust, which is clearly cratered in this view, the blue is the water, and the green is the water-air interface. The asteroid came in from the right. Note the higher crown on the downstream side (the side opposite the impact trajectory).

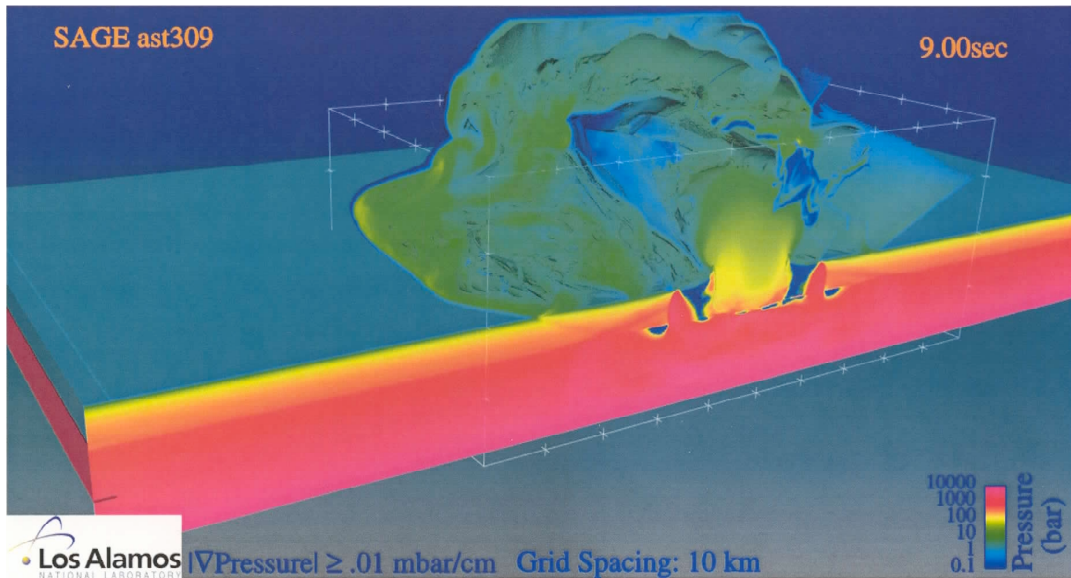


Figure 3. A pressure isosurface plot from a run of a 30 degree impactor, otherwise similar to the run depicted in Figures 1 and 2. The bolide came in from the right, and the expanding pressure wave is strongly enhanced in the downstream direction.

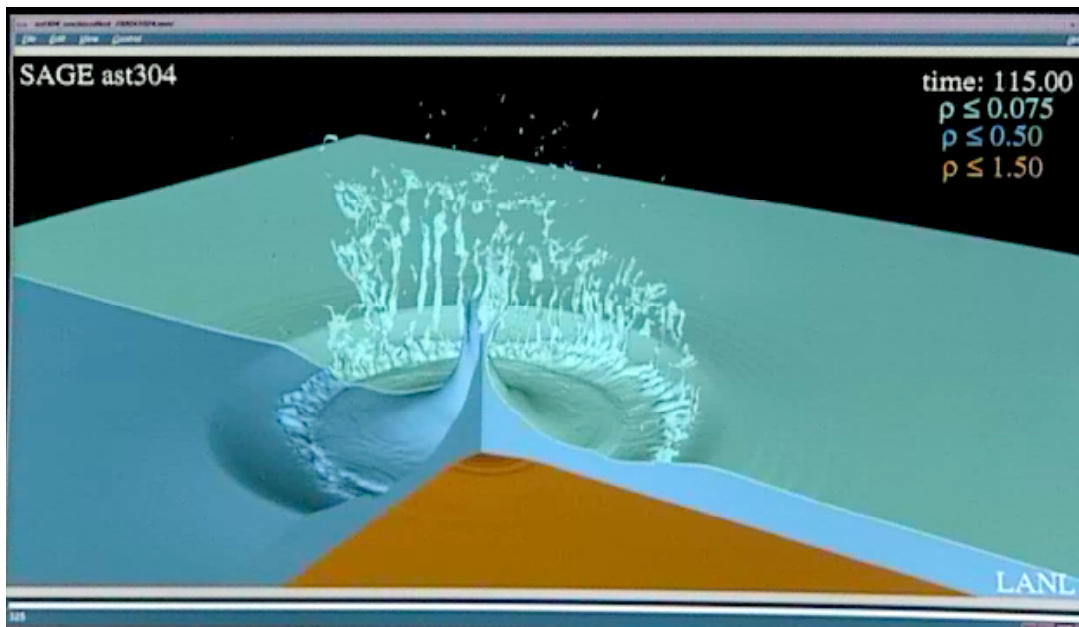


Figure 4. Similar to Fig. 2, but during the time of formation of the central vertical jet. Much of the initial asymmetry is now washed out. The collapse of the crown has produced a circular rim wave that is propagating out in all directions, but the principal tsunami wave will be produced by the collapse of the central vertical jet.

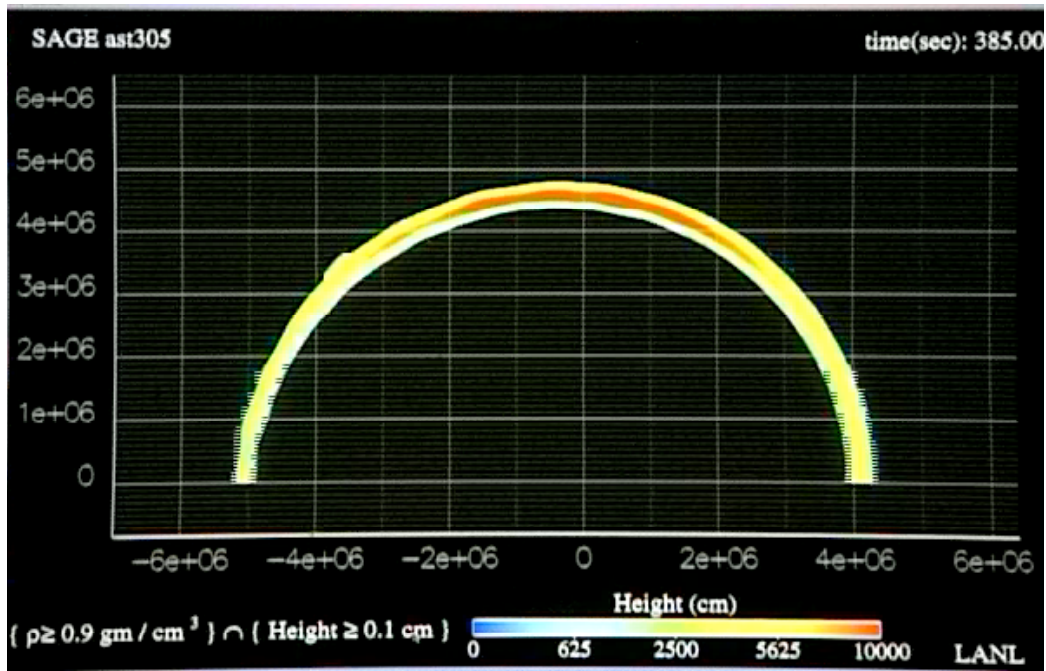


Figure 5. Overhead plot at late time showing the tsunami height as a function of x , the direction along the trajectory, and y , the direction perpendicular to the trajectory. The asteroid entered from the right. At 385 seconds, the maximum wave height is roughly 100 meters, at a distance of 40 km from the impact point.

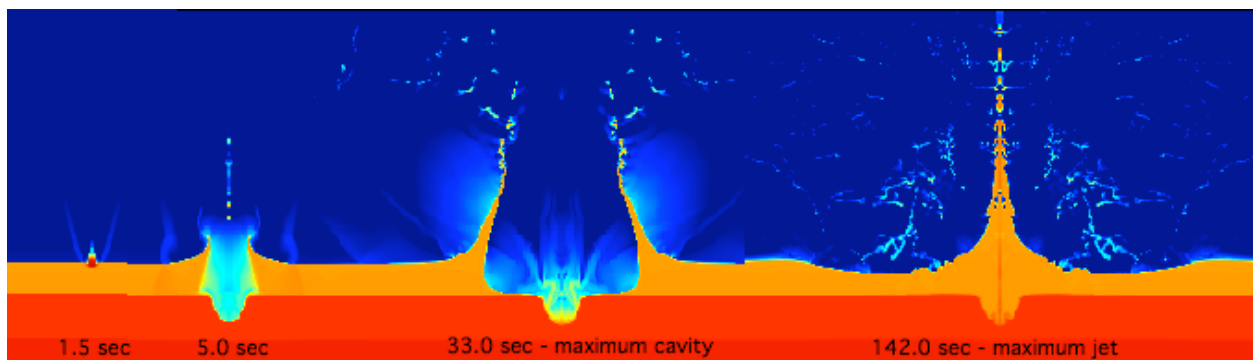


Figure 6. A 1-km iron vertical impactor craters the basalt crust, excavates a cavity in the ocean 25 km diameter, makes a vertical jet 40 km high, and a tsunami of initial amplitude 1.2 km. The excavation of the basalt is considerably greater than in the 45-degree impact, because much less of the asteroid's kinetic energy is dissipated in the water. The jetting is also considerably enhanced.

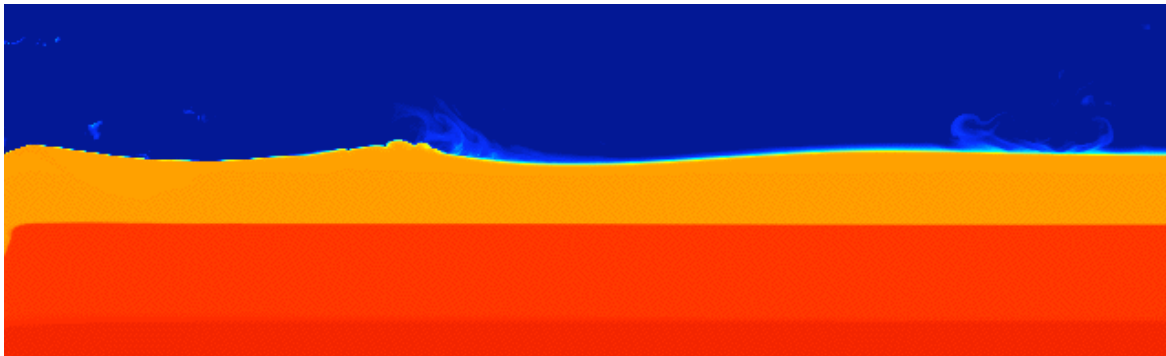
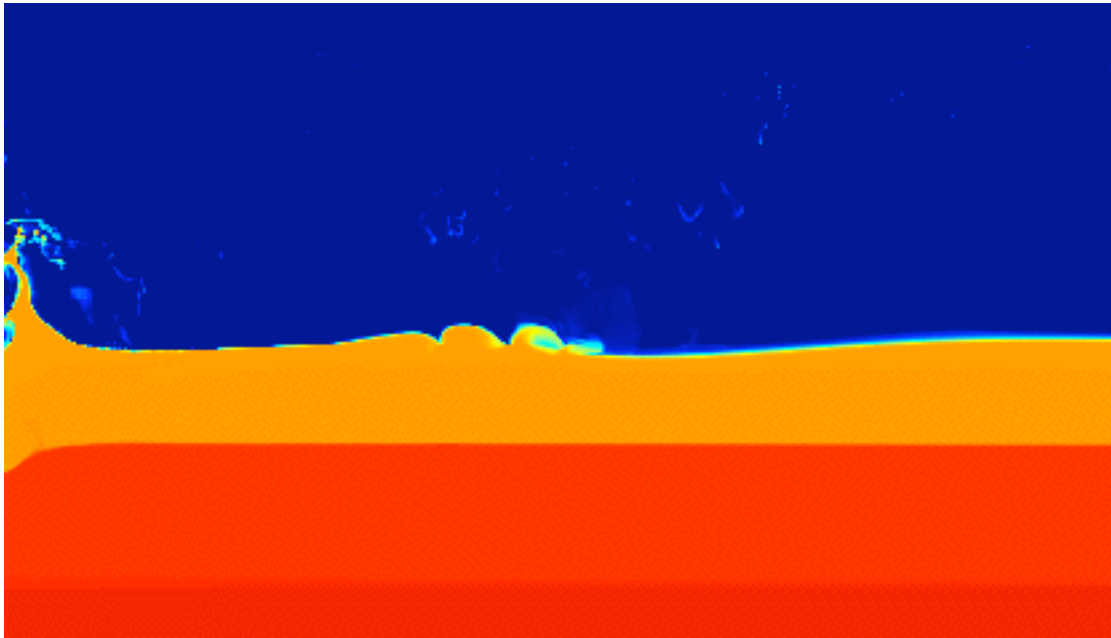


Figure 7. Portions of density plots from two different runs, shortly after the collapse of the transient crater, illustrating the complexity of the wave train. The phenomena are influenced by reflections and interactions of multiple shocks propagating through the water and the basalt crust.

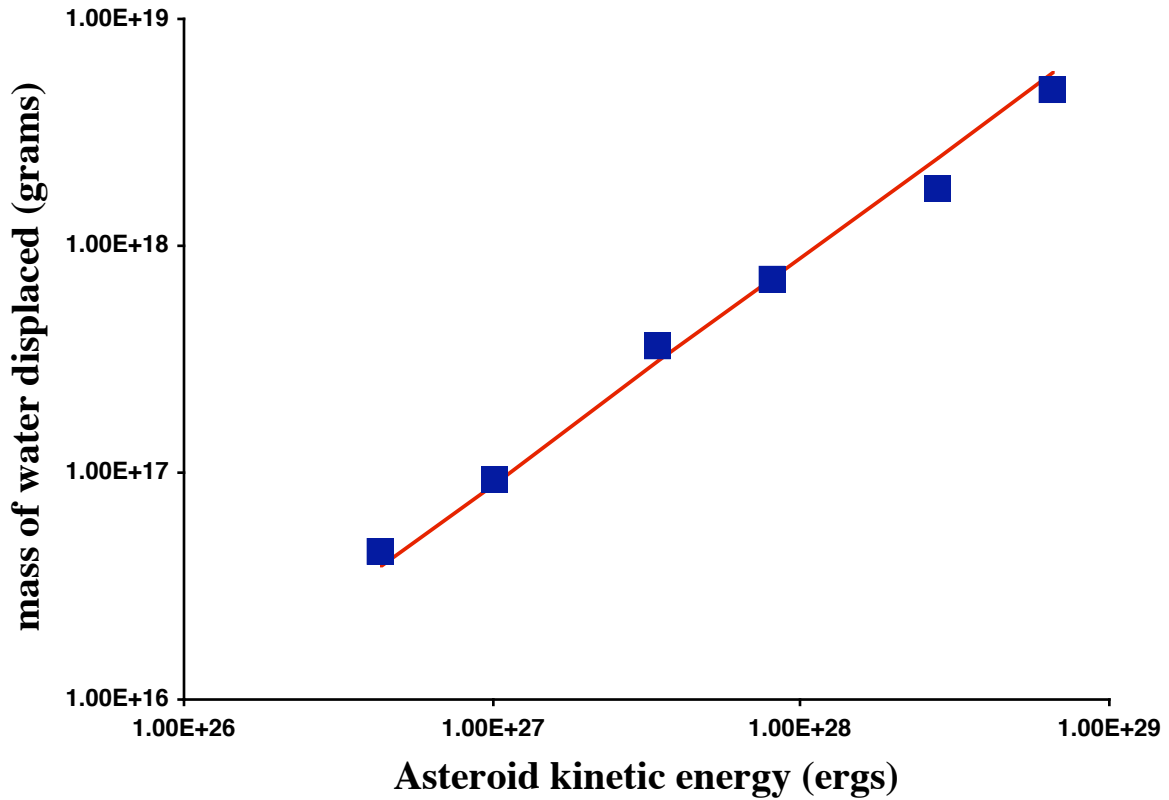


Figure 8. The mass of water displaced in the initial cavity formation scales with the asteroid kinetic energy. The squares are the results from the parameter-study simulations, as tabulated in Table I, and the solid line simply illustrates direct proportionality. A fraction (~5-20%) of this mass is vaporized in the initial encounter.

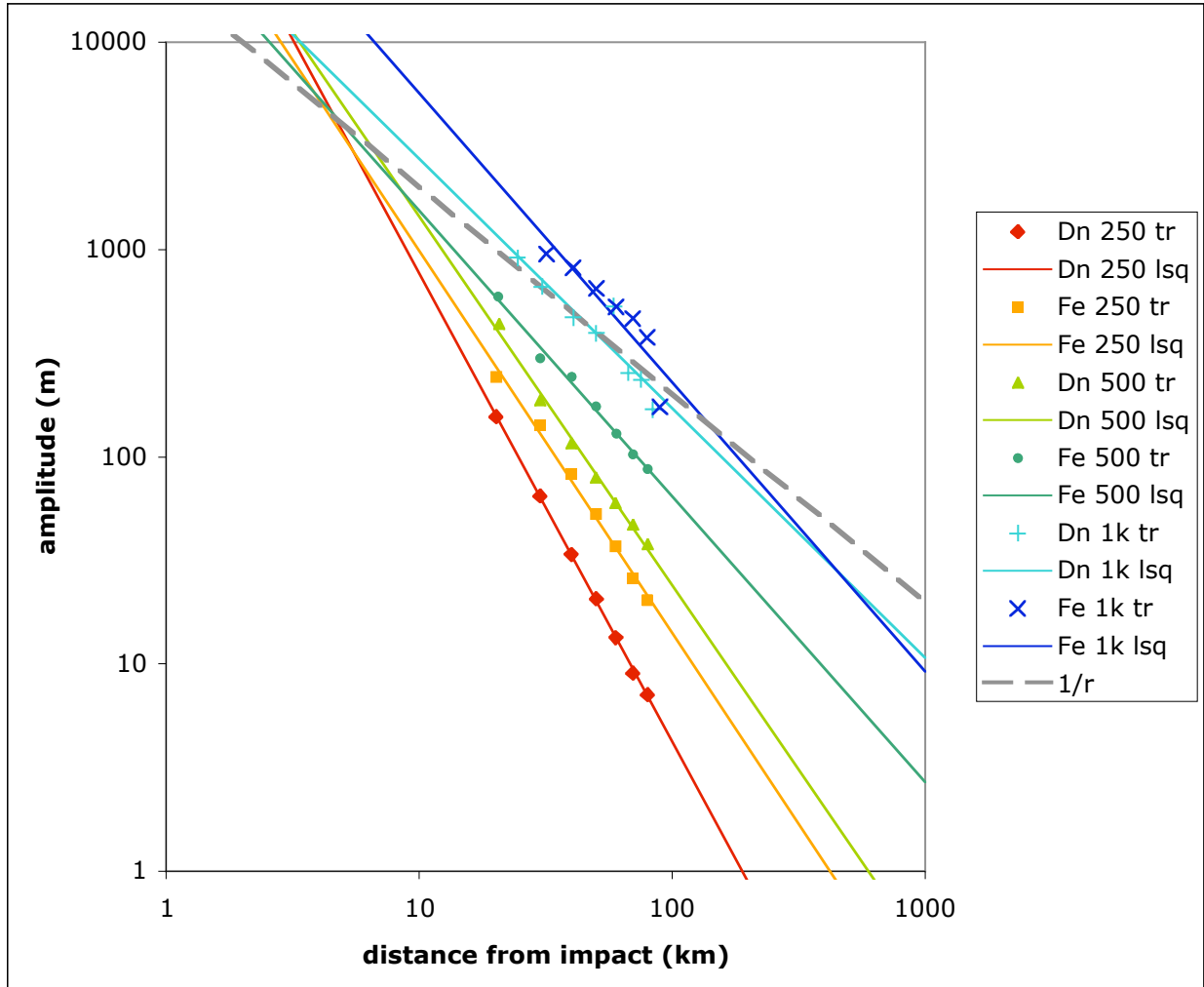


Figure 9. The tsunami amplitude scales roughly with kinetic energy and declines with distance somewhat faster than $1/r$. The legend identifies the points associated with individual runs, where the notation signifies the asteroid composition (“Dn” for dunitite and “Fe” for iron) and diameter in meters. For all impactors, the amplitudes were measured from tracer particles advected with the flow. Each series of points is fitted with a least-squares power-law fit whose line is also shown in the plot. The power-law indices varied from -2.25 to -1.3 .

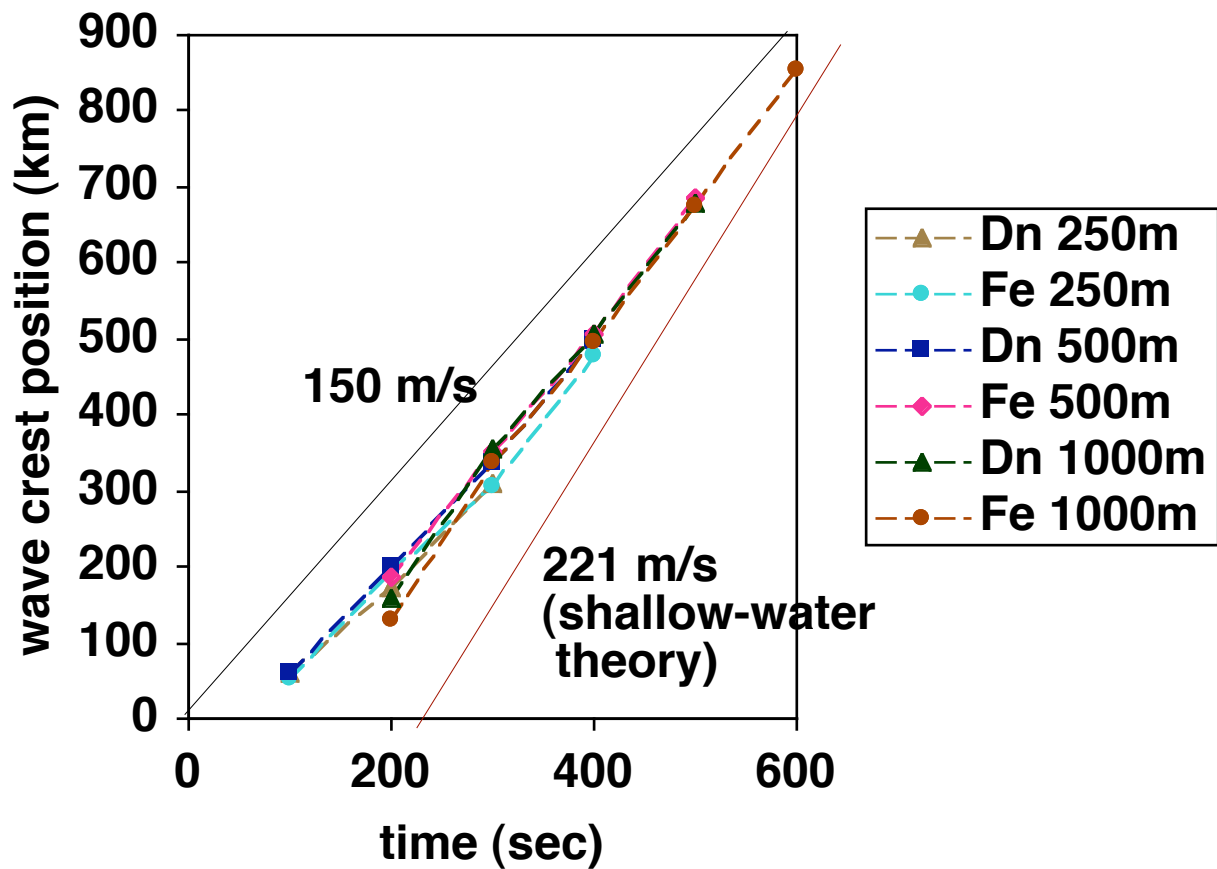


Figure 10. The tsunami wave crest positions as a function of time is here plotted for the six runs of the parameter study. The notation in the legend is the same as for Figure 8, with the solid lines at constant velocity to illustrate that these waves are substantially slower than the shallow-water theory prediction. There is an indication, however, that the waves may be accelerating towards the shallow-water limit at late times.

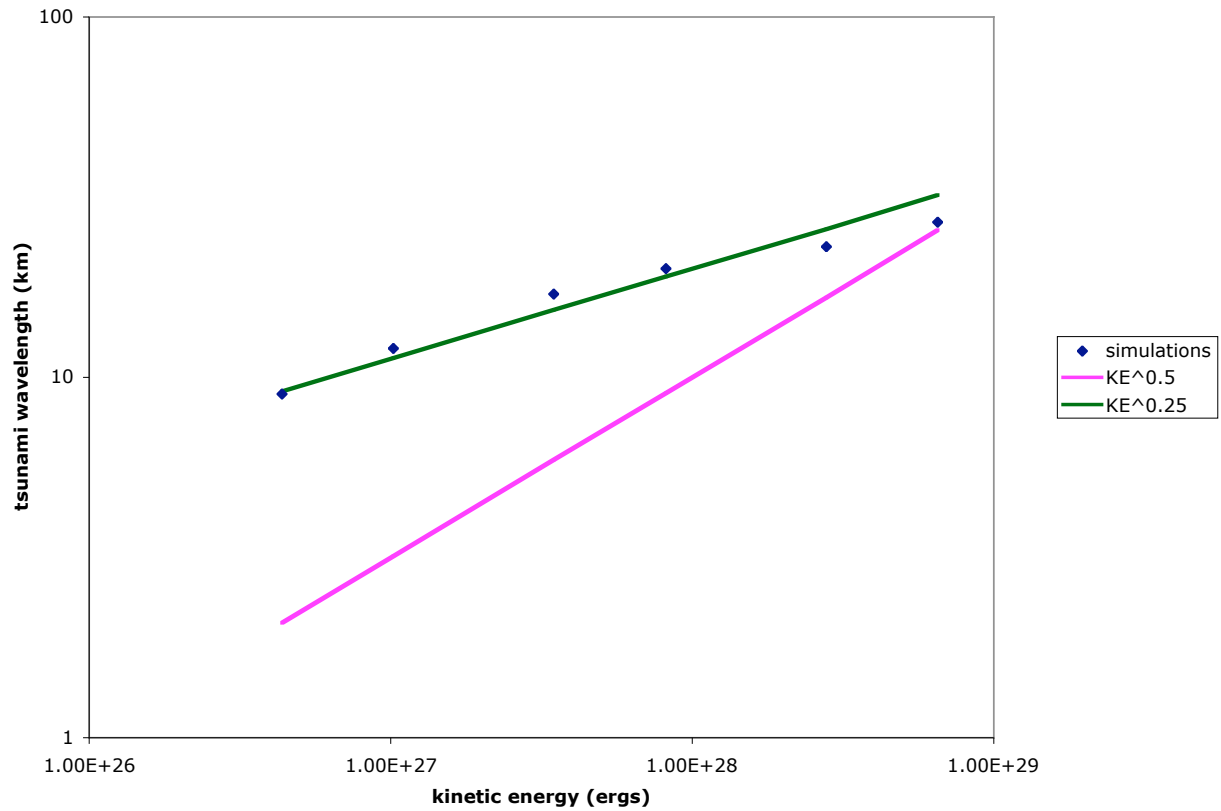


Figure 11. The tsunami wavelength as a function of the kinetic energy of the impacting asteroid. Points are from the simulations of the parameter study, as detailed in Table I, and the lines are to illustrate scalings. We find that the wavelength scales roughly with the 1/4 power of the asteroid's kinetic energy.